Reaction Mechanism and Kinetics of Oxygen Reduction Reaction on the Iron-Nickel Dual Atom Catalyst

Journal:	*Journal of Materials Chemistry A*
Manuscript ID	TA-ART-09-2023-005694.R1
Article Type:	Paper
Date Submitted by the Author:	12-Oct-2023
Complete List of Authors:	Tamtaji, Mohsen; Hong Kong University of Science and Technology Li, Yuyin; The Hong Kong University of Science and Technology Cai, Yuting; The Hong Kong University of Science and Technology, Department of Chemical and Biological Engineering Liu, Hongwei; Hong Kong University of Science and Technology Goddard III, William; California Institute of Technology Chen, GuanHua; The University of Hong Kong, Chemistry; Hong Kong Quantum AI Lab Limited

Reaction Mechanism and Kinetics of Oxygen Reduction Reaction on the Iron-Nickel Dual Atom Catalyst

Mohsen Tamtaji[1], Yuyin Li[2], Yuting Cai[2], Hongwei Liu[2], William A. Goddard III[3]*, GuanHua Chen[1,4]*

[1]Hong Kong Quantum AI Lab Limited, Pak Shek Kok, Hong Kong SAR, China

[2]Department of Chemical and Biological Engineering, Guangdong-Hong Kong-Macao Joint Laboratory for Intelligent Micro-Nano Optoelectronic Technology, William Mong Institute of Nano Science and Technology, and Hong Kong Branch of Chinese National Engineering Research Center for Tissue Restoration and Reconstruction, The Hong Kong University of Science and Technology, Clear Water Bay, Kowloon, Hong Kong, 999077, P.R. China

[3]Materials and Process Simulation Center (MSC), MC 139-74, California Institute of Technology, Pasadena CA, 91125, USA

[4]Department of Chemistry, The University of Hong Kong, Pokfulam Road, Hong Kong SAR, China

*Corresponding Authors, email: ghc@everest.hku.hk and wag@caltech.edu

1   **Abstract**

2   Dual-atom catalysts (DACs) have recently emerged as promising and high-activity catalysts for

3   the oxygen reduction reaction (ORR), a key process in many electrochemical energy conversion

4   devices. However, the ORR mechanism and kinetics on DACs has not yet been established. To

5   address this problem, we employed grand canonical potential kinetics (GCP-K) with CANDLE

6   solvation. The behavior of the free energy and grand canonical potential for ORR and hydrogen

7   evolution reaction (HER) intermediates (OO*, OOH*, O*, OH*, and H*) and their corresponding

8   transition states at constant charges were calculated and converted to free energy as a function of

9   applied potential to predict current density as a function of applied potential for ORR (through the

10   associative pathway) and the competitive HER on iron-nickel DAC (FeNiN6-DAC). We find a

11   Tafel slope of 281 mV/dec for ORR, comparable with the experimental Tafel slope of 169 mV/dec

12   at the current density of -1.7 mA/cm^2. The change in concentration of ORR reaction intermediates

13   on FeNiN6-DAC as a function of applied potentials indicates that the dominant intermediate is

14   OH* at potentials > 0.25 V vs. RHE. The charge transfer and spin density of Fe active sites reaches

15   a maximum during each proton transfer steps. The partial density of states of 3d orbitals on the

16   Fe site indicates that the $3d_{x2-y2}$ orbital is near the Fermi level, while the position of the $3d_{z2}$ orbital

17   and Fermi level decreases along the first reaction step of $OO^* \xrightarrow{H^+} OOH^*$. These insights into the

18   fundamental aspects of ORR on DACs provide guidance for the design of efficient catalysts.

19   **Keywords:** grand canonical potential kinetics, GCP-K, jDFTx, Tafel slope, spin

1 **1. Introduction**

2 Efficient oxygen reduction reaction (ORR) to ensure rapid reaction kinetics is a crucial process in

3 many electrochemical energy conversion devices, including fuel cells, metal-air batteries, and

4 electrolyzers [1,2]. In ORR, the dioxygen is reduced through the OOH*, O*, and OH* reaction

5 intermediates to produce two water molecules *via* the four-electron transfer pathway and/or a H_2O_2

6 molecule *via* a two-electron transfer pathway, as shown in **Scheme 1** [3–5], typically occurring at

7 the cathode of these devices. But a major bottleneck for the commercialization of DACs is the

8 sluggish kinetics and the competition with the hydrogen evolution reaction (HER) as shown in

9 **Scheme 1** [6,7]. Therefore, to develop new catalysts with high efficiency and rapid reaction

10 kinetics toward ORR, there is an urgent need to investigate the fundamentals behind their reaction

11 mechanism.

12 Dual atom catalysts (DACs) have recently attracted widespread interest towards high-performance

13 electrochemical reactions by enabling regulation of the electronic structure and spin state of the

14 metal centers [8–13]. Thus, co-doping a counterpart metal beside the active metal site can act as

15 electron donors to help stabilize the intermediate species in the reaction mechanism [14–16].

16 Previous studies have applied theoretical calculations and experimental synthesis to DACs for

17 various electrochemical applications such as CO_2 reduction reaction (CO_2RR), nitrogen reduction

18 reaction (NRR), HER, and ORR [17–24]. The theoretical studies for ORR have mainly reported

19 the Gibbs free energy (ΔG) of the main reaction intermediates such as H*, OH*, O*, OOH*, and

20 OO* at zero net charge with the goal of predicting the limiting potential (φ) and overpotential

21 (η=1.23-φ) [25–27]. In most calculations, the dependence of the Gibbs free energy of the

22 intermediates is assumed to be linear in the applied potential (U) as:

$$\Delta G_{OH^*}(U) = \Delta G_{OH^*}|_{at\ U\ =\ 0\ V} - eU \tag{1}$$

$$\Delta G_{O^*}(U) = \Delta G_{O^*}|_{at\ U = 0\ V} - 2eU \tag{2}$$

$$\Delta G_{OOH^*}(U) = \Delta G_{OOH^*}|_{at\ U = 0\ V} - 3eU \tag{3}$$

1   where e is the electron charge [28–30]. However, linear dependence is assumed and has been

2   shown to be incorrect in some studies [31,32]. In addition, the *zero-potential* Gibbs free energies

3   are generally assumed to be equal to the zero-charge values and the potential of zero charge (U_{PZC})

4   at which the system is neutral is assumed to be 0 V. However, it has been shown that the potential

5   of zero charge at neutral charges is higher than 0, and at zero potential, the intermediates are not

6   neutral [33]. Importantly, the transition states between the OO*, OOH*, O, OH*, and H*

7   intermediates are essential to provide an understanding of the ORR reaction mechanism and

8   kinetics on DACs. That is, we need to calculate the reaction barriers, reaction rates, charge transfer,

9   and spin population of active metal site along the proton transfer steps that give rise to the current-

10   potential (I-V) curve, Tafel slope, and the concentration of each reaction intermediate on the

11   catalyst's surface [34–36].

12   In addition, investigation of partial density of states along the proton transfer steps is needed to

13   understand the changes in molecular orbital configurations responsible for the evolution in

14   bonding interactions and Gibbs free energies. These aspects have been investigated partially for

15   several electrochemical reactions on various catalysts. For example, the reaction mechanism and

16   kinetics of CO_2 reduction to CO on nickel single atom catalyst (SAC) was examined, indicating

17   that the rate-determining step is the proton transfer to CO_2 [33]. In addition, the mechanism and

18   predicted kinetics as a function of applied potential for NRR and HER for the iron-ruthenium DAC

19   was reported, leading to the onset potential of -0.22 V vs. Reversible Hydrogen Electrode (RHE)

20   at the current density of 10 mAcm^{-2} for ammonia synthesis [32].

1   In this work, we employ DFT calculations to examine ORR and HER mechanisms on iron-nickel

2   DAC (FeNiN6-DAC). We use VASPsol code to perform structural relaxation for OO*, OOH*,

3   O*, OH*, and H* intermediates, and the climbing image nudged elastic band (CI-NEB) calculation

4   for calculating transition states between the reaction intermediates. Then we used the joint DFT

5   calculations with CANDLE solvation to calculate the free energy of reaction intermediates and

6   transition states at constant charges ($n-n_0$=0, 0.5, 1, and 1.5 e⁻). Applying a Legendre

7   transformation, converts the constant-charge free energies to constant-potential free energies

8   which was used to calculate reaction rates as a function of applied potential. The behavior of free

9   energy, grand canonical potential, charge transfer, spin population, and density of states of Fe

10   metal was investigated along the reaction pathway. The resulting I-V curve and Tafel slopes for

11   ORR and HER were calculated and compared with experimental results in the literature. The

12   change in the concentration of ORR reaction intermediates on the Fe active site of FeNiN6-DAC

13   indicates that at high potentials the proton transfer to OH* to producer water is the rate limiting

14   step, while at low potentials the proton transfer to O* to producer OH* is the rate limiting step.

15

16   **2. Grand canonical potential kinetics formulation**

17   **2.1 Structural relaxation and free energy calculations**

18   In this study, we used a combination of spin-polarized DFT calculations and solvation models to

19   investigate ORR mechanism on the FeNiN6-DAC. The calculations were performed using the

20   Vienna ab initio Simulation Package (VASP, version 5.4.4) and jDFTx (version 1.7.0) software.

21   The relaxed structure of the reaction intermediates were calculated using the VASPsol solvation

22   code in VASP at constant charge using the PBE functional. The climbing image nudged elastic

23   band (CI-NEB) method was then employed in the VTST package to obtain the relaxed structure

1   of transition states as a function of net charges ($n-n_0$) using VASPsol solvation code. The DFT-D3

2   method was used to account for London dispersion (van der Waals attraction) interactions [37].

3   To describe the explicit polarization effect involved in proton transfer events, we added three

4   explicit water molecules to the reaction system and performed the structural relaxation in VASPsol

5   with a default dielectric constant of $\varepsilon=78.4$ for water [32][33][34]. It is worth mentioning that

6   introducing only three explicit water molecules into the systems in the vertical direction, might not

7   fully describe the influence of the dynamic hydrogen bond network and might have some impacts

8   on the calculated reaction barriers. In fact, the hydrogen dynamic transfer can happen between

9   more than three water molecules in other directions. As shown in **Figure 1a**, a 4×4 supercell of

10   graphene was constructed (12.8 Å×12.8 Å), and an iron-nickel pair was placed at the four carbon

11   vacancies and coordinated with six N atoms (FeNiN6-DAC). A 20 Å vacuum space was added

12   along the z direction to avoid any interaction between periodic images, the Brillouin zone was

13   sampled by the 4×4×1 Monkhorst-Pack k-point scheme, and the energy cutoff was set at 500 eV.

14   The convergence criteria were set as 10^{-6} eV in energy and 0.02 eVÅ^{-1} in force for the structure

15   relation of intermediates while the convergence criteria were set as 10^{-8} eV in energy and 0.05

16   eVÅ^{-1} in force for CI-NEB calculations for the structure relation of transition states.

17   To obtain single-point free energy of reaction intermediates and transition states, the VASP-

18   optimized stagnation point at a series of constant charges was recalculated in jDFTx. The constant-

19   charge free energy was then transformed to constant-potential free energy through the Legendre

20   transformation. The CANDLE solvation model was used for all single-point free energy

21   calculations with chemical potential of an electron ($\mu_{e,SHE}=4.66$ eV) at the standard hydrogen

22   electrode (SHE). The reference Fermi energy of the electron was corrected by 0.0592×pH. All e

1   single-point free energy calculations used a plane wave basis set with a 4×4×1 k-point mesh and

2   energy cutoff of 20 Hartree, and the free energy convergence was set to the default 10^{-8} Hartree.

3

4   **2.2 Legendre transformation**

5   Our recently developed GCP-K methodology can be used to determine the kinetics for

6   heterogenous electrochemistry as a function of net charges and applied potential while allowing

7   the transition states to evolve continuously. GCP-K uses a Legendre transformation to convert the

8   fixed-charge single-point free energy in jDFTx code, *F(n)*, to grand canonical, *G(n;U)*, allowing

9   the thermodynamic free energy for heterogeneous electrochemical reactions to depend on the

10   applied potential (*U*). The derivation starts with the general definition of the grand canonical

11   potential [38]:

$$G(n;U) = F(n) - ne(U_{SHE} - U) \qquad (4)$$

12   where *G* is the grand canonical free energy, which depends on the number of electrons (*n*), the

13   applied potential (*U* vs. SHE), the. total free energy (*F(n)*), and the electronic energy ($U_{SHE} =$

14   $\mu_{e,SHE}/e$) at SHE conditions. The sign of *U* is defined as the potential used in experiments,

15   i.e., *U*= -0.7 V corresponds to -0.7 V vs. SHE. We calculate how the number of electrons depends

16   on the applied potential to obtain *G(n;U)* as a thermodynamic potential. To do this, we shift the

17   Fermi level to correspond to the applied potential by changing the electronic band occupation,

18   varying the number of electrons in the systems (equation 4). Finally, we obtain *GCP(U)* through

19   minimizing *G(n;U)* according to [38]:

$$\frac{dG(n;U)}{dn} = 0 \ \text{ or } \ \mu_{e,SHE} = \frac{dF(n)}{dn} = e(U_{SHE} - U) \qquad (5)$$

20   Minimizing *G(n;U)* leads to a quadratic form in *GCP(U)*. To obtain *GCP(U)* we fit a quadratic

21   expansion of *F(n)* [33]:

$$F(n) = a(n - n_0)^2 + b(n - n_0) + c \tag{6}$$

1   where a, b, and c $(=F(n=n_0))$ are determined from fitting. So, the grand canonical potential is as

2   follows [39]:

$$G(n;U) = a(n - n_0)^2 + (b - (U_{SHE} - U))(n - n_0) + c + n_0 e(U_{SHE} - U) \tag{7}$$

3   Minimization of grand canonical potential leads to [39]:

$$GCP(U) = -\frac{1}{4a}(b - \mu_{e,SHE} + eU)^2 + c - n_0 \mu_{e,SHE} + n_0 eU \tag{8}$$

4   The parameter a is related to the Differential capacitance, $C_{diff} = \frac{\partial n}{\partial U} = -\frac{1}{2a}$, while the parameter

5   b is related to the potential of zero charge, $U_{PZC} = b/e - \mu_{e,SHE}/e$. Since at the potential of zero

6   charge, the system is neutral, $n(U_{PZC}) = n_0$, we can write $U - U_{PZC} = \frac{1}{C_{diff}}(n - n_0)$. So [39]:

$$n(U) = -\frac{1}{e}\frac{\partial GCP(U)}{\partial U} = n_0 - \frac{1}{2ae}(b - \mu_{e,SHE} + eU_{PZC}) \tag{9}$$

7   Thus, we can write, $b = \mu_{e,SHE} - eU_{PZC}$. Putting these physical quantities into equations 4 and 5,

8   we write the free energy and grand canonical potential as follows [39]:

$$F(n) = -\frac{1}{2C_{diff}}(n - n_0)^2 + (\mu_{e,SHE} - eU)(n - n_0) + F_0 \tag{10}$$

$$GCP(U) = -\frac{e^2 C_{diff}}{2}(U - U_{PZC})^2 + n_0 eU + F_0 - n_0 \mu_{e,SHE} \tag{11}$$

9   where, n_0 is the number of electrons at zero net charge (total number of valence electron), $\mu_{e,SHE}$ is

10   the chemical potential of an electron versus SHE, and e is the energy in eV. This quadratic form

11   of free energy $F(n)$ and grand canonical potential $GCP(U)$ accounts for the change in capacitance

12   as the potential changes [33].

13

3. Results and Discussion

We have investigated the reaction mechanism of oxygen reduction reaction (ORR) in both four-

electron transfer pathway ($O_2 \xrightarrow{H^+} OOH^* \xrightarrow{H^+} O^* + H_2O \xrightarrow{H^+} OH^* + H_2O \xrightarrow{H^+} 2H_2O$) and the two-

electron transfer pathway ($O_2 \xrightarrow{H^+} OOH^* \xrightarrow{H^+} H_2O_2$) along with the competitive HER ($H^+ \xrightarrow{} \frac{1}{2}H_2$)

on FeNiN6-DAC which the reaction steps are shown in **Scheme 1**. **Figure 1a** shows top and side

view of the optimized structure model of FeNiN6-DAC. Fe and Ni are anchored on the moiety

side and the bond lengths are denoted in Å. As shown in **Figure 1b**, we used DFT calculations in

the VASP package for structure relaxation of the intermediates and the CI-NEB calculations for

structure relaxation of transition states at constant charges ($n-n_0=0$, 0.5, 1, and 1.5 e$^-$). Then, we

used single point calculations in jDFTx package to calculate constant charge free energies under

CANDLE solvation. The Legendre transformation was then used to convert the fixed-charge free

energies to the fixed-potential free energies and to convert the free energy (*F(n)*) to grand canonical

potential (*GCP(U)*) and reaction barriers. Next, reaction rates, current densities, and concentration

of reaction intermediates were calculated.

As shown in **Figure S1**, adsorption of dioxygen which is the first step of ORR on FeNiN6-DAC

can be *via* either end-on or side-on orientation and can lead to either associative or enzymatic

pathways, respectively. The calculated adsorption free energy at the potential of zero charge

(*U=U_PZC* and *n=n_0*) is -0.85 eV lower for the end-on configuration and because it is not an

electrochemical step, the effect of applied potential is assumed to be negligible on the

O_2 adsorption. This indicates that end-on configuration (associative pathway) on FeNiN6-DAC is

far more favorable than side-on configuration (enzymatic pathway) for all the potentials. This also

indicates that Fe acts as an active metal center and Ni acts only as the electron donor providing

electronic modulation to the Fe site, in agreement with previous reports [14]. This can be explained

1   by the fact that the adsorption of dioxygen on Ni single atom site is very weak compared to Fe site

2   [40]. When the O_2 binds *via* the end-on configuration, the O-O bond elongates from its nominal

3   value of 1.24 Å to 1.29 Å. **Figure 1c** indicates graphical description of the ORR intermediates in

4   which three explicit water molecules was added to the reaction system to describe the explicit

5   polarization effect involved in proton transfers and **Figure S2** displays free energy changes at

6   applied potentials of 1 and 0.2 V vs. RHE through associative pathway on Fe active site of FeNiN6-

7   DAC, as shown in **Figure 1c**.

8   The geometry and free energy level of six transition states was investigated between each

9   intermediate steps of *ab* ($OO^* \xrightarrow{H^+} OOH^*$), *bc* ($OOH^* \xrightarrow{H^+} O^* + H_2O$), *cd* ($O^* \xrightarrow{H^+} OH^*$), *da* ($OH^*$

10   $\xrightarrow{H^+} H_2O$), *ae* ($* \xrightarrow{H^+} H^*$), and *ef* ($H^* \xrightarrow{H^+} H_2$). Then, we considered the behavior of the free energy

11   and grand canonical potential as a function of the number of electrons for each reaction

12   intermediate and their corresponding transition states. For example, **Figure 2a** demonstrates the

13   free energies (*F(n)*) of FeNiN6-DAC bonded with OO* *via* end-on configuration as a function of

14   number of net electrons of system ($n-n_0$), indicates a nearly linear relationship. The blue dots and

15   dash curve denote the DFT calculated energies and polynomial 2nd order fitting, respectively. The

16   reported free energy (*F(n)*) contains four different parts as follows:

$$F(n) = E_{tot}(n) + E_{ZPE}(n) - E_{TS}(n) - E_{solvent}(n) \tag{12}$$

17   Which *$E_{tot}(n)$* is the total energy of the system, *$E_{ZPE}(n)$* and *$E_{TS}(n)$* are the zero-point energy and

18   entropy contributions, respectively, and *$E_{solvent}(n)$* is single-point solvation energy correction.

19   *$E_{tot}(n)$*, *$E_{TS}(n)$* and *$E_{solvent}(n)$* are obtained from single point energy calculations in the jDFTx code

20   using CANDLE solvation. The zero-point energy contribution (*$E_{ZPE}(n)$*) for each reaction

21   intermediate including the three free water molecules is obtained from the vibrational frequency

22   calculation in the VASP package along with VASPsol code to include the contributions of phonon

1   frequency at T=298 K. The zero-point energy contribution of FeNiN6-DAC as the adsorption sites

2   is assumed to be negligible. Based on the 2nd order polynomial fit of free energy ($F(n)$) versus net

3   charges, we can calculate the differential capacitance, $C_{diff} = \frac{\partial n}{\partial U} = -\frac{1}{2 \times 0.6509} = -0.7682$

4    $electron^2/eV$ and potential of zero charge of $U_{PZC}=0.9318$ V. The differential capacitance

5   indicates that the capacitance of the electrode interface decreases by 0.7682 units for each unit

6   increase in electrode potential. **Table S1** shows the fitting parameters obtained from quadratic

7   fitting of $F(n)$ versus net charge to obtain the grand canonical potential along with differential

8   capacitance and potential of zero charge for all the reaction intermediates and their correspondence

9   transition state.

10   As shown in **Figure 2b**, when the energy contribution of each electron at SHE is subtracted from

11   total free energy ($F(n)-n\mu_{e,SHE}$), the relation between free energy and number of electrons becomes

12   quadratic with a minimum at the net charge of $n-n_0=0.7158$ e^-. In fact, this quadratic dependence

13   leads to the optimum number of electrons for each potential. As shown in **Figure 2c**, when an

14   external potential is applied to the system, the free energy minimum is shifted toward higher

15   electron numbers of n-n$_0$=1.3303 e$^-$, ensuring that the reaction progresses in the forward direction.

16   **Figure S3a** indicates the dependence of the number of net electrons of the system as a function

17   of applied potential, suggesting a linear relationship with R^2 value of 1 and slope of $C_{diff} = \frac{-1}{2a}$

18   $= -0.7682$ $electron/V$ and intercept value of $C_{diff}U_{PZC}=0.7158$ V. **Figure 2d** displays the

19   polynomial dependence of the grand canonical potential $GCP(U)$ as a function of applied potential

20   for FeNiN6-DAC bonded to OO* with R^2 value of 1 and an equation as follows:

$$GCP(U) = -\frac{e^2 C_{diff}}{2}U^2 + \left(n_0 + (n - n_0)_{at\ U\ =\ 0}\right)eU + GCP(U = 0) = -0.3841U^2 + 245.7158U - 17005.4716 \tag{13}$$

1   So, the reaction barrier for step ab ($OO\overset{*}{}\xrightarrow{H^+}OOH\overset{*}{}$) is shown in **Figure S3b** and can be written

2   as:

$$G^{\ddagger}_{ab} = 0.0313U^2 + 0.0625U + 0.4543 \tag{14}$$

3   As shown in **Figure 3a**, to form OOH* when the OO is chemisorbed to Fe active site *via* end-side

4   configuration, we introduce three water molecules (H_6O_3) to the system. The proton in the

5   H_6O_3 cluster reacts with the OO* molecule to form the OOH* intermediate while producing a

6   cluster of 2 solvated H_2O molecules and one solvated OH ion. Four images (01-04) were inserted

7   to search for TS, where 00 and 05 indicate the reactant and product, respectively, *via* the minimum

8   energy path (MEP). The dashed green lines are shown to clarify the atom displacement along the

9   reaction pathway. **Figure 3a** and **Figures S4-8** show the reaction pathway of steps ab ($OO\overset{*}{}\xrightarrow{H^+}$

10   $OOH\overset{*}{}$), bc ($OOH\overset{*}{}\xrightarrow{H^+}O\overset{*}{} + H_2O$), cd ($O\overset{*}{}\xrightarrow{H^+}OH\overset{*}{}$), da ($OH\overset{*}{}\xrightarrow{H^+}H_2O$), ae ($\overset{}{*}\xrightarrow{H^+}H\overset{*}{}$), and ef (

11   $H\overset{*}{}\xrightarrow{H^+}H_2$), indicating the optimized structures of the initial, transition, and final states at applied

12   potential of 1 V versus RHE. **Figure 3b** shows the free energy barrier for the step ab ($OO\overset{*}{}\xrightarrow{H^+}$

13   $OOH\overset{*}{}$) at different numbers of net electrons ($n-n_0$) in the system. This shows the maximum energy

14   barrier of 0.5 eV and 1.4 eV at net charge of $n-n_0=0\ e^-$ for the conversion of $OO\overset{*}{}\xrightarrow{H^+}OOH\overset{*}{}$ in

15   forward and backward directions, respectively, on Fe site of FeNiN6-DAC. **Figure 3c** shows the

16   O-H bond distance variation of TS 03 of step ab, indicating the increase in the bond length at more

17   negative potentials. Based on our calculations, the transition state moves towards final state as

18   more negative potential applied indicating the forward direction of reaction progresses.

19   The proton transfer from three water molecules to OOH* intermediate can go through two different

20   pathways: (i) formation of HOOH* intermediate to produce H_2O_2 *via* a two-electron reaction

21   pathway and (ii) formation of O* intermediate and H_2O water *via* a four-electron reaction pathway

1   (**Scheme 1**). As shown in **Figure S2**, the energy level of O* is lower than the energy level of

2   HOOH* suggesting that the four-electron reaction pathway is more favorable on FeNiN6-DAC

3   than the two-electron reaction pathway.

4   In addition, we investigated the charge transfer and spin of the Fe active site. **Figure 4a-b** show

5   the charge transfer and spin of Fe along the reaction pathway of step ab ($OO^* \xrightarrow{H^+} OOH^*$) at the

6   applied potential of 1 V versus RHE. This indicates the increase in both charge transfer and spin

7   along the proton transfer. **Figure 4c-d** shows the contour plot of charge transfer and spin of system

8   vs. net electrons and reaction pathway of $OO^* \xrightarrow{H^+} OOH^*$. The transition state TS 03 of step ab

9   shows the highest charge transfer and spin density at Fe. The charge transfer for steps bc (OOH^*

10    $\xrightarrow{H^+} O^* + H_2O$), cd ($O^* \xrightarrow{H^+} OH^*$), and da ($OH^* \xrightarrow{H^+} H_2O$) along the reaction pathway applied

11   potential of 1 V versus RHE is shown in **Figures S12-15**. This indicates the increase in charge

12   transfer along the proton transfer.

13   The density of states (DOS) of Fe atom in FeNiN6-DAC system for initial and final states of step

14   ab ($OO^* \xrightarrow{H^+} OOH^*$) is shown in **Figure 5a**, indicating the presence of the d_{x2-y2} orbital of Fe atom

15   at the Fermi level. **Figure 5b** shows the position of the d_{z2} orbital and Fermi level along the reaction

16   pathway of step ab ($OO^* \xrightarrow{H^+} OOH^*$), indicating that both decrease along the proton transfer with

17   a minimum at the TS 03. **Figure 5c** shows the molecular orbital of 3d orbital of free Fe and Fe-

18   OO* active metal at the initial, transition, and final states of step ab ($OO^* \xrightarrow{H^+} OOH^*$). By

19   comparing the molecular orbital of free FeNiN6-DAC with FeNiN6-DAC bonded to OO*, we see

20   that d_{x2-y2} and d_{z2} goes to lower and higher energy states, respectively, after the adsorption of OO*.

21   This also indicates that d_{xy} orbital is empty, d_{x2-y2} and d_{z2} orbitals are singly occupied, and d_{xz} and

22   d_{yz} orbitals are doubly occupied. The spin crossover can also happen during the proton transfer (

1   $OO^* \xrightarrow{H^+} OOH^*$) where Fe goes from the triplet state to the doublet state with an empty d_{z2}.

2   **Figures S17** and **S18** show the band structure and partial density of states (PDOS) analysis of the

3   initial and final states of step ab $OO^* \xrightarrow{H^+} OOH^*$. In both initial and final states, there are bonding

4   and antibonding orbitals on d_{xy}, d_{x2-y2}, and d_{z2}. The biggest change during the proton transfer is on

5   the d_{z2} orbital, suggesting that this orbital participates in the hybridization.

6   We predict the free energy reaction barriers based on GCP(U). **Figure 6a** shows the schematic

7   representation of free energies at 298.15 K and pH 0 and applied potentials of 1 V (blue) and 0.2 V

8   vs. RHE (red). This summarizes all reaction intermediates (*a-f*) and transition state (TS) free

9   energies involved in the reduction of O_2 on FeNiN6-DAC at 1 V and 0.2 V constant applied

10 potential. In order to calculate the concentration of each intermediate on Fe active site and current

11 density versus applied potential, the following equations are taken into accounts [41]:

$$\frac{dx_a}{dt} = -(k_{ab} + k_{ae})x_a + (k_{ba} + k_{ba'})x_b + k_{da}x_d + k_{ea}x_e + k_{fa}x_f \tag{15}$$

$$\frac{dx_b}{dt} = k_{ab}x_a - (k_{ba'} + k_{ba} + k_{bc})x_b + k_{cb}x_c \tag{16}$$

$$\frac{dx_c}{dt} = k_{bc}x_b - (k_{cb} + k_{cd})x_c + k_{dc}x_d \tag{17}$$

$$\frac{dx_d}{dt} = k_{cd}x_c - (k_{dc} + k_{da})x_d \tag{18}$$

$$\frac{dx_e}{dt} = k_{ae}x_a + k_{fe}x_f - (k_{ea} + k_{ef})x_e \tag{19}$$

$$\frac{dx_f}{dt} = k_{ef}x_e - (k_{fe} + k_{fa})x_f \tag{20}$$

12 where k_{ij} is the reaction rate for reaction step ij, which is calculated from the Eyring rate equation

13 as follows [41]:

$$k_{ij}(U) = \frac{k_B T}{h} exp\left(-\frac{\Delta G_{ij}^{\ddagger}(U)}{k_B T}\right) \qquad (21)$$

1   where $\Delta G_{ij}^{\ddagger}(U)$ is the reaction barrier for the reaction step ij, while k_B, T, and h are Boltzmann

2   constant, temperature, and Planck's constant, respectively. The current density and concentrations

3   are calculated at the steady state condition in which $\frac{dx_a}{dt} = \frac{dx_b}{dt} = \frac{dx_c}{dt} = \frac{dx_d}{dt} = \frac{dx_e}{dt} = \frac{dx_f}{dt} = 0$. The

4   concentrations are normalized based on $\sum_{i=a}^{f} x_i = 1$.

5   **Figure 6b** shows calculated current densities for ORR and HER on FeNiN6-DAC versus applied

6   potential along with experimental data ORR from ref. 12 (green line) for comparison. We find that

7   the direct four-electron transfer pathway is dominant under low applied potentials, while the HER

8   pathway becomes more favorable at higher applied potentials. The Tafel slope represents the rate

9   of change of the current density with respect to the applied potential and can be used to determine

10   and compare the kinetic parameters of the ORR reaction. **Figure 6c** displays Tafel slope of 281

11   calculated from the I-V curve for ORR on FeNiN6-DAC, comparable with the experimental Tafel

12   slope of 169 mV/dec for ORR from ref. [14] (green line). The discrepancy between the Tafel slope

13   obtained from computational calculations and experimental results might be due to the sluggish

14   kinetics of ORR. In addition, other possible reasons for this discrepancy can be due to the

15   limitations on the DFT calculations such as the pseudopotential and number of explicit waters.

16   Therefore, the agreement between the DFT- and experimental-obtained Tafel slopes might be

17   improved by using a more accurate pseudopotential than PBE and considering more explicit waters

18   in several directions to consider the accurate dynamic hydrogen transfer towards more accurate

19   reaction barriers and reaction kinetics [36]. **Figure 6c** displays also the Tafel slope of 61 mV/dec

20   calculated from the I-V curves for HER on FeNiN6-DAC. This Tafel slope is comparable with the

21   experimental HER Tafel slope of 129 mV/dec, shown in **Figure S19**, for Fe single atom catalyst

1   (FeN4-SAC) from ref. [42]. **Figure 7** shows the change in the concentration of ORR reaction

2   intermediates on the Fe active site of FeNiN6-DAC at different potentials indicating the dominant

3   coverage of surface with OH* intermediate at higher potentials. This shows that at higher

4   potentials, the desorption of OH* intermediate to produce H_2O is the rate limiting step, while the

5   proton transfer to O* to produce OH* intermediate is the rate limiting step at low potentials, in

6   agreement with previous reports [26].

7

8   **4. Conclusion**

9   In this paper, we employed grand canonical potential kinetics (GCP-K) to study the reaction

10   mechanism and kinetics for ORR through the associative pathway and its competitive hydrogen

11   evolution reaction (HER) on iron-nickel dual atom catalyst (FeNiN6-DAC). The behavior of the

12   free energy and grand canonical potential is investigated using CANDLE solvation in joint DFT

13   calculations for reaction intermediates (OO*, OOH*, O*, OH*, and H*) and their corresponding

14   transition states at constant potentials. Investigation of the $OO^* \xrightarrow{H^+} OOH^*$ step, reveals that the

15   charge transfer and spin density of Fe reaches a maximum during the proton transfer. The Tafel

16   slope of 281 mV/dec calculated from the I-V curves for ORR, comparable with the experimental

17   Tafel slope of 169 mV/dec. The change in the concentration of ORR reaction intermediates on the

18   Fe active site of FeNiN6-DAC at various potentials indicates that OH* and O* are the dominant

19   intermediates at potentials > 0.25 V and < 0.25 V vs. RHE, respectively. Our study aimed to

20   provide insights into the fundamental aspects of ORR on DACs and to guide the design of more

21   efficient ORR catalysts.

22

23   **Acknowledgments**

4

Associated Content

Supporting Information

Grand canonical potential kinetics and density of states (Word)

8

Author contributions

Mohsen Tamtaji: conceptualization, DFT calculations, and writing. *Yuyin Li*: Conceptualization and analysis. *Yuting Cai*: Conceptualization and analysis. *Hongwei Liu*: Conceptualization and writing. *William A. Goddard III*: Supervision, conceptualization, and editing *GuanHua Chen*: Supervision, conceptualization, and editing.

Conflicts of interest

The authors respectfully declare that there are no conflicts of interest to acknowledge for this research.

References

[1]   X. Li, Z. Xiang, Identifying the impact of the covalent-bonded carbon matrix to FeN4 sites for acidic oxygen reduction, Nat. Commun. 13 (2022). https://doi.org/10.1038/s41467-021-27735-1.

[2]   Z. Xu, G. Chen, F. Yang, J. Jang, G. Liu, F. Xiao, Y. Sun, X. Qiu, W. Chen, D. Su, M. Gu, M. Shao, Graphene-supported Fe/Ni single atoms and FeNi alloy nanoparticles as bifunctional oxygen electrocatalysts for rechargeable zinc-air batteries, Electrochim. Acta. 458 (2023) 142549. https://doi.org/10.1016/j.electacta.2023.142549.

[3]   H.A. Hansen, V. Viswanathan, J.K. NØrskov, Unifying kinetic and thermodynamic analysis of 2 e- and 4 e - reduction of oxygen on metal surfaces, J. Phys. Chem. C. 118 (2014) 6706–6718. https://doi.org/10.1021/jp4100608.

[4]   J. Zhang, A. Yu, C. Sun, Computational Exploration of Dual Atom Catalysts Loaded on Defective Graphene for Oxygen Reduction Reaction, Appl. Surf. Sci. (2022) 154534. https://doi.org/10.1016/j.apsusc.2022.154534.

[5]   F. Xiao, Q. Wang, G.L. Xu, X. Qin, I. Hwang, C.J. Sun, M. Liu, W. Hua, H. wen Wu, S. Zhu, J.C. Li, J.G. Wang, Y. Zhu, D. Wu, Z. Wei, M. Gu, K. Amine, M. Shao, Atomically dispersed Pt and Fe sites and Pt–Fe nanoparticles for durable proton exchange membrane fuel cells, Nat. Catal. 5 (2022) 503–512. https://doi.org/10.1038/s41929-022-00796-1.

[6]   H. Xu, D. Cheng, D. Cao, X.C. Zeng, A universal principle for a rational design of single-atom electrocatalysts, Nat. Catal. 1 (2018) 339–348. https://doi.org/10.1038/s41929-018-0063-z.

[7]   W. Fang, Y. Wu, S. Xin, Y. Hu, J. Dang, M. Li, B. Chen, H. Zhao, Z. Li, Fe and Mo dual-site single-atom catalysts for high-efficiency wide-pH hydrogen evolution and alkaline overall water splitting, 468 (2023). https://doi.org/10.1016/j.cej.2023.143605.

[8]   F. Rehman, S. Kwon, C.B. Musgrave, M. Tamtaji, W.A. Goddard III, Z. Luo, High-throughput screening to predict highly active dual-atom catalysts for electrocatalytic reduction of nitrate to ammonia, Nano Energy. 103 (2022) 107866. https://doi.org/10.1016/j.nanoen.2022.107866.
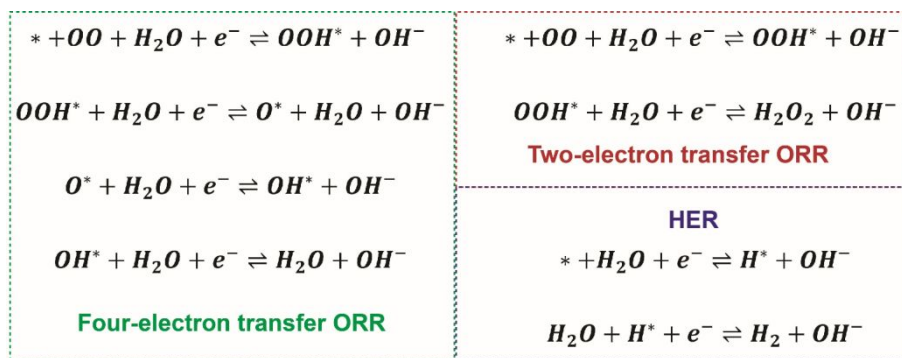
1   [9]   J. Shan, C. Ye, Y. Jiang, M. Jaroniec, Y. Zheng, S.Z. Qiao, Metal-metal interactions in

2   correlated single-atom catalysts, Sci. Adv. 8 (2022).

3   https://doi.org/10.1126/sciadv.abo0762.

4   [10]   J. Wang, C.X. Zhao, J.N. Liu, Y.W. Song, J.Q. Huang, B.Q. Li, Dual-atom catalysts for

5   oxygen electrocatalysis, Nano Energy. 104 (2022) 107927.

6   https://doi.org/10.1016/j.nanoen.2022.107927.

7   [11]   F. Kong, M. Wang, Y. Huang, G. Meng, M. Chen, H. Tian, Y. Chen, C. Chen, Z. Chang,

8   X. Cui, J. Shi, Cu-N-bridged Fe-3d electron state regulations for boosted oxygen reduction

9   in flexible battery and PEMFC, Energy Storage Mater. 54 (2023) 533–542.

10   https://doi.org/10.1016/j.ensm.2022.11.003.

11   [12]   Z. Chen, X. Su, J. Ding, N. Yang, W. Zuo, Q. He, Z. Wei, Q. Zhang, J. Huang, Y. Zhai,

12   Boosting oxygen reduction reaction with Fe and Se dual-atom sites supported by nitrogen-

13   doped porous carbon, Appl. Catal. B Environ. 308 (2022) 121206.

14   https://doi.org/10.1016/j.apcatb.2022.121206.

15   [13]   Q. Xue, Y. Wang, M. Jiang, R. Cheng, K. Li, T. Zhao, C. Fu, Engineering Electronic Spin

16   State of a CoNi Alloy for an Efficient Oxygen Reduction Reaction, (2023) 2–10.

17   https://doi.org/10.1021/acsaem.2c03831.

18   [14]   M. Tamtaji, Q. Peng, T. Liu, X. Zhao, Z. Xu, P. Ryan, D. Hossain, Z. Liu, H. Wong, H.

19   Liu, K. Amine, Y. Zhu, W.A. Goddard III, W. Wu, Z. Luo, Non-bonding interaction of

20   dual atom catalysts for enhanced oxygen reduction reaction, Nano Energy. 108 (2023)

21   108218. https://doi.org/10.1016/j.nanoen.2023.108218.

22   [15]   Y. Yan, X. Zheng, X. Li, Y. Yao, Y. Liu, Vibronic Coupling of Adjacent Single-Atom Co

23   and Zn Sites for Bifunctional Electrocatalysis of Oxygen Reduction and Evolution

24   Reactions, J. Phys. Chem. Lett. 13 (2022) 2548–2554.

25   https://doi.org/10.1021/acs.jpclett.2c00209.

26   [16]   J. Du, G. Han, W. Zhang, L. Li, Y. Yan, Y. Shi, X. Zhang, L. Geng, Z. Wang, Y. Xiong,

27   G. Yin, C. Du, CoIn dual-atom catalyst for hydrogen peroxide production via oxygen

28   reduction reaction in acid, Nat. Commun. 14 (2023) 4766. https://doi.org/10.1038/s41467-

1   023-40467-8.

2   [17] W. Liu, L. Ding, M. Liu, X. Wang, Z. Zhang, T. Jiang, Unraveling the interfacial effect of
3   PdBi bimetallic catalysts on promoting CO 2 electroreduction to formate Template for
4   Preparation of Manuscripts for Nano Research, (2023).

5   [18] X. Han, X. Ling, D. Yu, D. Xie, L. Li, S. Peng, C. Zhong, N. Zhao, Y. Deng, W. Hu,
6   Atomically Dispersed Binary Co-Ni Sites in Nitrogen-Doped Hollow Carbon Nanocubes
7   for Reversible Oxygen Reduction and Evolution, Adv. Mater. 31 (2019).
8   https://doi.org/10.1002/adma.201905622.

9   [19] Y. Cheng, S. He, J.P. Veder, R. De Marco, S. ze Yang, S. Ping Jiang, Atomically
10   Dispersed Bimetallic FeNi Catalysts as Highly Efficient Bifunctional Catalysts for
11   Reversible Oxygen Evolution and Oxygen Reduction Reactions, ChemElectroChem. 6
12   (2019) 3478–3487. https://doi.org/10.1002/celc.201900483.

13   [20] Q. An, J. Jiang, W. Cheng, H. Su, Y. Jiang, Q. Liu, Recent Advances in Dual-Atom Site
14   Catalysts for Efficient Oxygen and Carbon Dioxide Electrocatalysis, Small Methods. 6
15   (2022) 1–19. https://doi.org/10.1002/smtd.202200408.

16   [21] L. Sun, V. Reddu, X. Wang, Multi-atom cluster catalysts for efficient electrocatalysis,
17   Chem. Soc. Rev. (2022) 8923–8956. https://doi.org/10.1039/d2cs00233g.

18   [22] L. Jiao, J. Zhu, Y. Zhang, W. Yang, S. Zhou, A. Li, C. Xie, X. Zheng, W. Zhou, S. Yu, H.
19   Jiang, Non-Bonding Interaction of Neighboring Fe and Ni Single-Atom Pairs on MOF-
20   Derived N‑Doped Carbon for Enhanced CO 2 Electroreduction, (2021).
21   https://doi.org/10.1021/jacs.1c08050.

22   [23] R. Cepitis, N. Kongi, J. Rossmeisl, V. Ivaništšev, Surface Curvature Effect on Dual-Atom
23   Site Oxygen Electrocatalysis, ACS Energy Lett. 8 (2023) 1330–1335.
24   https://doi.org/10.1021/acsenergylett.3c00068.

25   [24] L. Bai, C.S. Hsu, D.T.L. Alexander, H.M. Chen, X. Hu, Double-atom catalysts as a
26   molecular platform for heterogeneous oxygen evolution electrocatalysis, Nat. Energy. 6
27   (2021) 1054–1066. https://doi.org/10.1038/s41560-021-00925-3.

28   [25] G. Yang, J. Zhu, P. Yuan, Y. Hu, G. Qu, B.A. Lu, X. Xue, H. Yin, W. Cheng, J. Cheng,

1   W. Xu, J. Li, J. Hu, S. Mu, J.N. Zhang, Regulating Fe-spin state by atomically dispersed

2   Mn-N in Fe-N-C catalysts with high oxygen reduction activity, Nat. Commun. 12 (2021)

3   4–13. https://doi.org/10.1038/s41467-021-21919-5.

4 [26] T. Liu, Y. Wang, Y. Li, How pH Affects the Oxygen Reduction Reactivity of Fe-N-C

5   Materials, ACS Catal. 13 (2023) 1717–1725. https://doi.org/10.1021/acscatal.2c05540.

6 [27] Z. Xiao, P. Sun, Z. Qiao, K. Qiao, H. Xu, S. Wang, D. Cao, Atomically dispersed Fe-Cu

7   dual-site catalysts synergistically boosting oxygen reduction for hydrogen fuel cells,

8   Chem. Eng. J. 446 (2022) 137112. https://doi.org/10.1016/j.cej.2022.137112.

9 [28] K. Khan, X. Yan, Q. Yu, S.H. Bae, J.J. White, J. Liu, T. Liu, C. Sun, J. Kim, H.M. Cheng,

10   Y. Wang, B. Liu, K. Amine, X. Pan, Z. Luo, Stone-Wales defect-rich carbon-supported

11   dual-metal single atom sites for Zn-air batteries, Nano Energy. 90 (2021) 106488.

12   https://doi.org/10.1016/j.nanoen.2021.106488.

13 [29] C. Fu, X. Qi, L. Zhao, T. Yang, Q. Xue, Z. Zhu, P. Xiong, J. Jiang, X. An, H. Chen, J.S.

14   Chen, A. Cabot, R. Wu, Synergistic cooperation between atomically dispersed Zn and Fe

15   on porous nitrogen-doped carbon for boosting oxygen reduction reaction, Appl. Catal. B

16   Environ. 335 (2023) 122875. https://doi.org/10.1016/j.apcatb.2023.122875.

17 [30] W. Yang, Z. Jia, B. Zhou, L. Wei, Z. Gao, H. Li, Surface states of dual-atom catalysts

18   should be considered for analysis of electrocatalytic activity, Commun. Chem. 6 (2023) 1–

19   7. https://doi.org/10.1038/s42004-022-00810-4.

20 [31] C.D. Taylor, M. Neurock, Theoretical insights into the structure and reactivity of the

21   aqueous/metal interface, Curr. Opin. Solid State Mater. Sci. 9 (2005) 49–65.

22   https://doi.org/10.1016/j.cossms.2006.03.007.

23 [32] F. Rehman, S. Kwon, M.D. Hossain, C.B. Musgrave, W.A. Goddard III, Z. Luo, Reaction

24   mechanism and kinetics for N2 reduction to ammonia on the Fe-Ru based dual-atom

25   catalyst, J. Mater. Chem. A. 461 (2022) 23323–23331.

26   https://doi.org/10.1039/d2ta06826e.

27 [33] M.D. Hossain, Y. Huang, T.H. Yu, W.A. Goddard III, Z. Luo, Reaction mechanism and

28   kinetics for CO2 reduction on nickel single atom catalysts from quantum mechanics, Nat.

1   Commun. 11 (2020) 1–14. https://doi.org/10.1038/s41467-020-16119-6.

2   [34] F. Li, H. Wen, Q. Tang, Reaction mechanism and kinetics for carbon dioxide reduction on
3   iron-nickel Bi-atom catalysts, J. Mater. Chem. A. 10 (2022) 13266–13277.
4   https://doi.org/10.1039/d2ta02931f.

5   [35] M.D. Hossain, Z. Liu, H. Liu, A. Tyagi, F. Rehman, J. Li, M. Amjadian, Y. Cai, W.A.
6   Goddard III, Z. Luo, The kinetics and potential dependence of the hydrogen evolution
7   reaction optimized for the basal-plane Te vacancy site of MoTe2, Chem Catal. 3 (2023)
8   100489. https://doi.org/10.1016/j.checat.2022.100489.

9   [36] C. Liu, J. Qian, Y. Ye, H. Zhou, C.J. Sun, C. Sheehan, Z. Zhang, G. Wan, Y.S. Liu, J.
10   Guo, S. Li, H. Shin, S. Hwang, T.B. Gunnoe, W.A. Goddard III, S. Zhang, Oxygen
11   evolution reaction over catalytic single-site Co in a well-defined brookite TiO2 nanorod
12   surface, Nat. Catal. 4 (2021) 36–45. https://doi.org/10.1038/s41929-020-00550-5.

13   [37] M. Tamtaji, S. Cai, W. Wu, T. Liu, Z. Li, H.Y. Chang, P.R. Galligan, S.I. Iida, X. Li, F.
14   Rehman, K. Amine, W.A. Goddard III, Z. Luo, Single and dual metal atom catalysts for
15   enhanced singlet oxygen generation and oxygen reduction reaction, J. Mater. Chem. A.
16   (2023). https://doi.org/10.1039/d2ta08240c.

17   [38] J. Song, S. Kwon, M.D. Hossain, S. Chen, Z. Li, W.A. Goddard III, Reaction Mechanism
18   and Strategy for Optimizing the Hydrogen Evolution Reaction on Single-Layer 1T′
19   WSe2and WTe2Based on Grand Canonical Potential Kinetics, ACS Appl. Mater.
20   Interfaces. 13 (2021) 55611–55620. https://doi.org/10.1021/acsami.1c14234.

21   [39] Y. Huang, R.J. Nielsen, W.A. Goddard III, Reaction Mechanism for the Hydrogen
22   Evolution Reaction on the Basal Plane Sulfur Vacancy Site of MoS 2 Using Grand
23   Canonical Potential Kinetics, J. Am. Chem. Soc. 140 (2018) 16773–16782.
24   https://doi.org/10.1021/jacs.8b10016.

25   [40] M. Tamtaji, S. Chen, Z. Hu, W.A. Goddard III, G. Chen, A Surrogate Machine Learning
26   Model for the Design of Single-Atom Catalyst on Carbon and Porphyrin Supports towards
27   Electrochemistry, (2023). https://doi.org/10.1021/acs.jpcc.3c00765.

28   [41] Y. Wang, Y. Li, T. Heine, PtTe Monolayer: Two-Dimensional Electrocatalyst with High

1   Basal Plane Activity toward Oxygen Reduction Reaction, J. Am. Chem. Soc. 140 (2018)

2   12732–12735. https://doi.org/10.1021/jacs.8b08682.

3   [42] K. Khan, T. Liu, M. Arif, X. Yan, M.D. Hossain, F. Rehman, S. Zhou, J. Yang, C. Sun,

4   S.H. Bae, J. Kim, K. Amine, X. Pan, Z. Luo, Laser-Irradiated Holey Graphene-Supported

5   Single-Atom Catalyst towards Hydrogen Evolution and Oxygen Reduction, Adv. Energy

6   Mater. 11 (2021) 2101619. https://doi.org/10.1002/aenm.202101619.

7

$$* + OO + H_2O + e^- \rightleftharpoons OOH^* + OH^-$$

$$OOH^* + H_2O + e^- \rightleftharpoons O^* + H_2O + OH^-$$

$$O^* + H_2O + e^- \rightleftharpoons OH^* + OH^-$$

$$OH^* + H_2O + e^- \rightleftharpoons H_2O + OH^-$$

Four-electron transfer ORR

$$* + OO + H_2O + e^- \rightleftharpoons OOH^* + OH^-$$

$$OOH^* + H_2O + e^- \rightleftharpoons H_2O_2 + OH^-$$

Two-electron transfer ORR

HER

$$* + H_2O + e^- \rightleftharpoons H^* + OH^-$$

$$H_2O + H^* + e^- \rightleftharpoons H_2 + OH^-$$

Scheme 1. Reaction steps. Reaction steps of four-electron transfer oxygen reduction reaction (ORR) and hydrogen evolution reaction (HER).
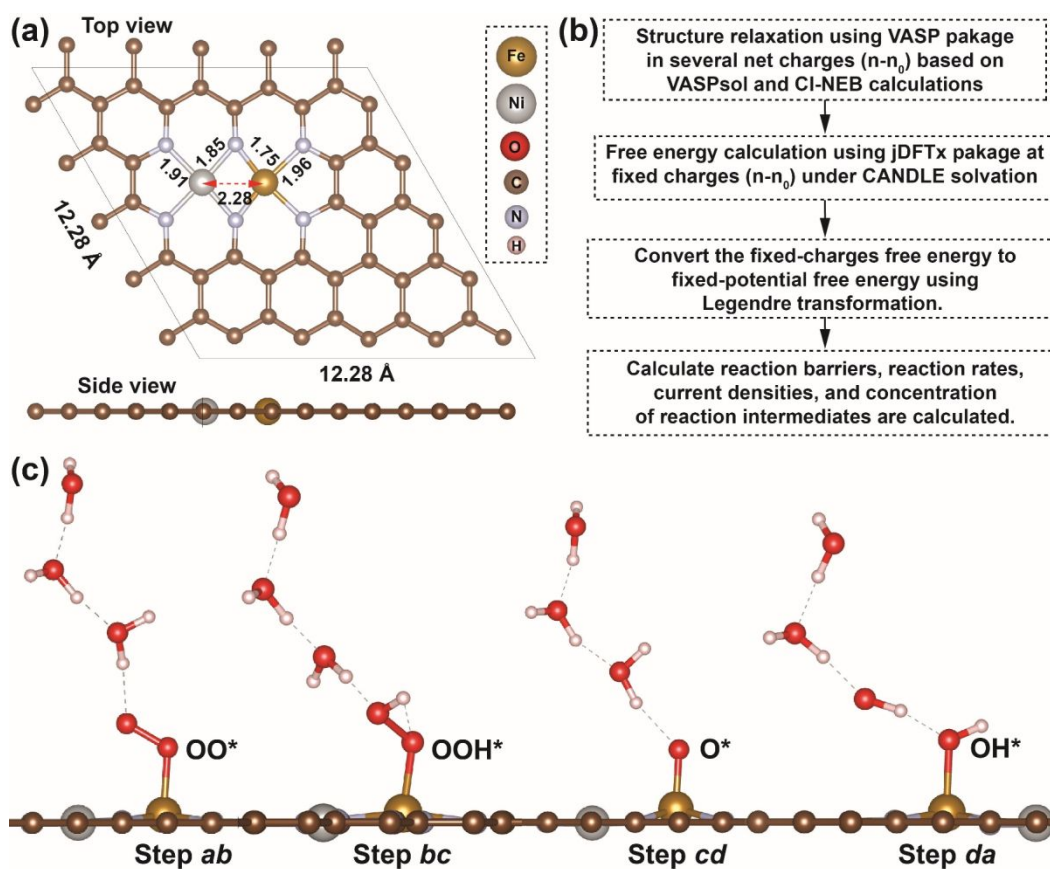
Figure 1. Oxygen reduction reaction (ORR) mechanism on FeNiN6-DAC. (a) Top and side view of the optimized structure model of FeNiN6-DAC (Dark gray color balls: carbon, gray: Iron, light blue: nitrogen, red: oxygen, salmon: hydrogen, and cream: nickel). Fe and Ni are anchored on the moiety side and the bond lengths are denoted in Å. (b) The overall calculation procedure of the GCP-K method. (c) Graphical description of the ORR pathway catalyzed by FeNiN6-DAC at the applied potential of 1 V vs. RHE.

1
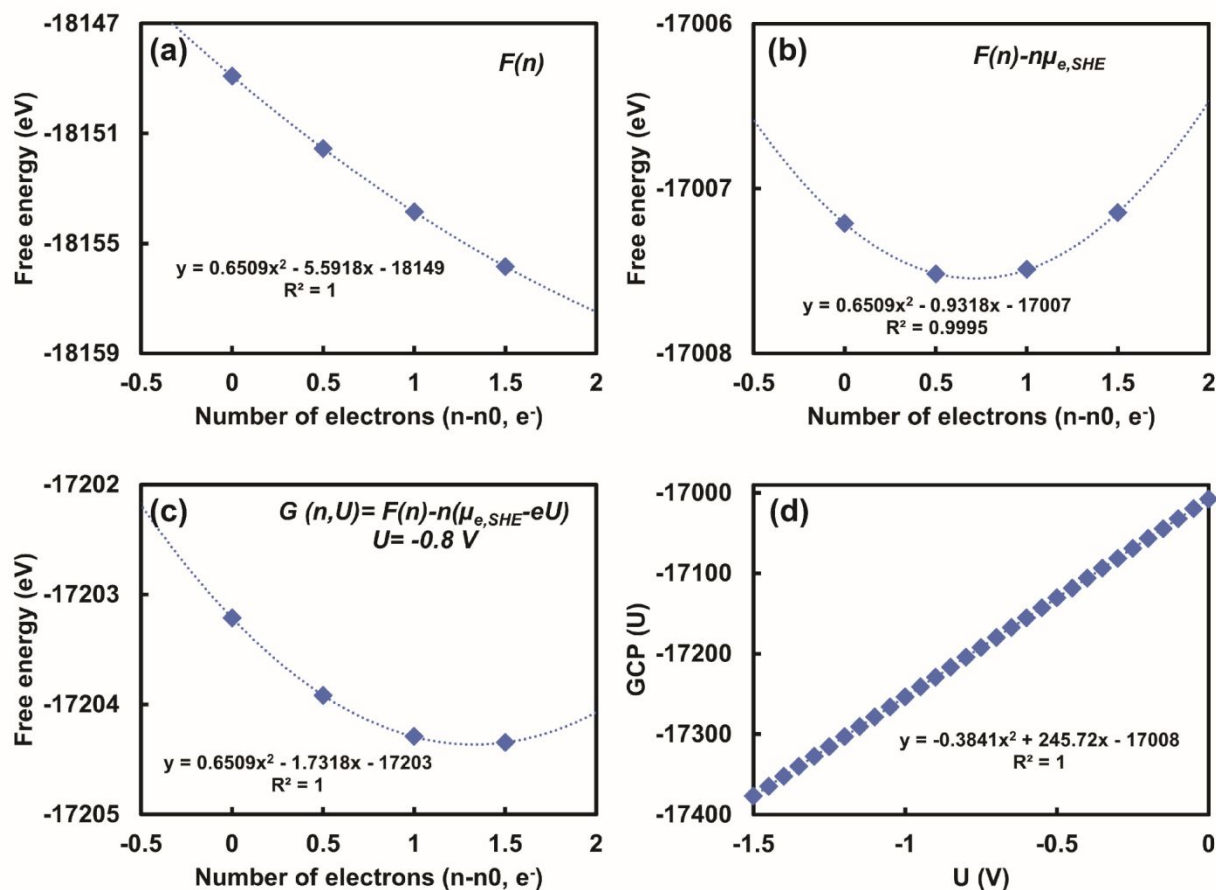
Figure 2. Behaviour of free energy and grand canonical potential as a function of the number of electrons. (a) The free energies of OO* bonded to FeNiN6-DAC a function of number of electrons $(n-n_0)$, indicates a nearly linear relationship. (b) The relation between free energy and number of net electrons becomes quadratic when the energy contribution of each electron at SHE is subtracted from total free energy. (c) Minimization of free energy as a function of number of net electrons when an external potential is applied to the system. The free energy minimum is shifted toward higher electron numbers as U is goes to more negative values, ensuring that the reaction progresses in the forward direction. The quadratic dependence allows the optimum number of electrons and grand canonical potential GCP(U) to be predicted for each U. (d) The dependence of the grand canonical potential GCP(U) as a function of applied potential for of FeNiN6-DAC bonded to OO*. The blue dots and dash curve denote the DFT calculated energies and polynomial 2nd order fitting, respectively.

1

2
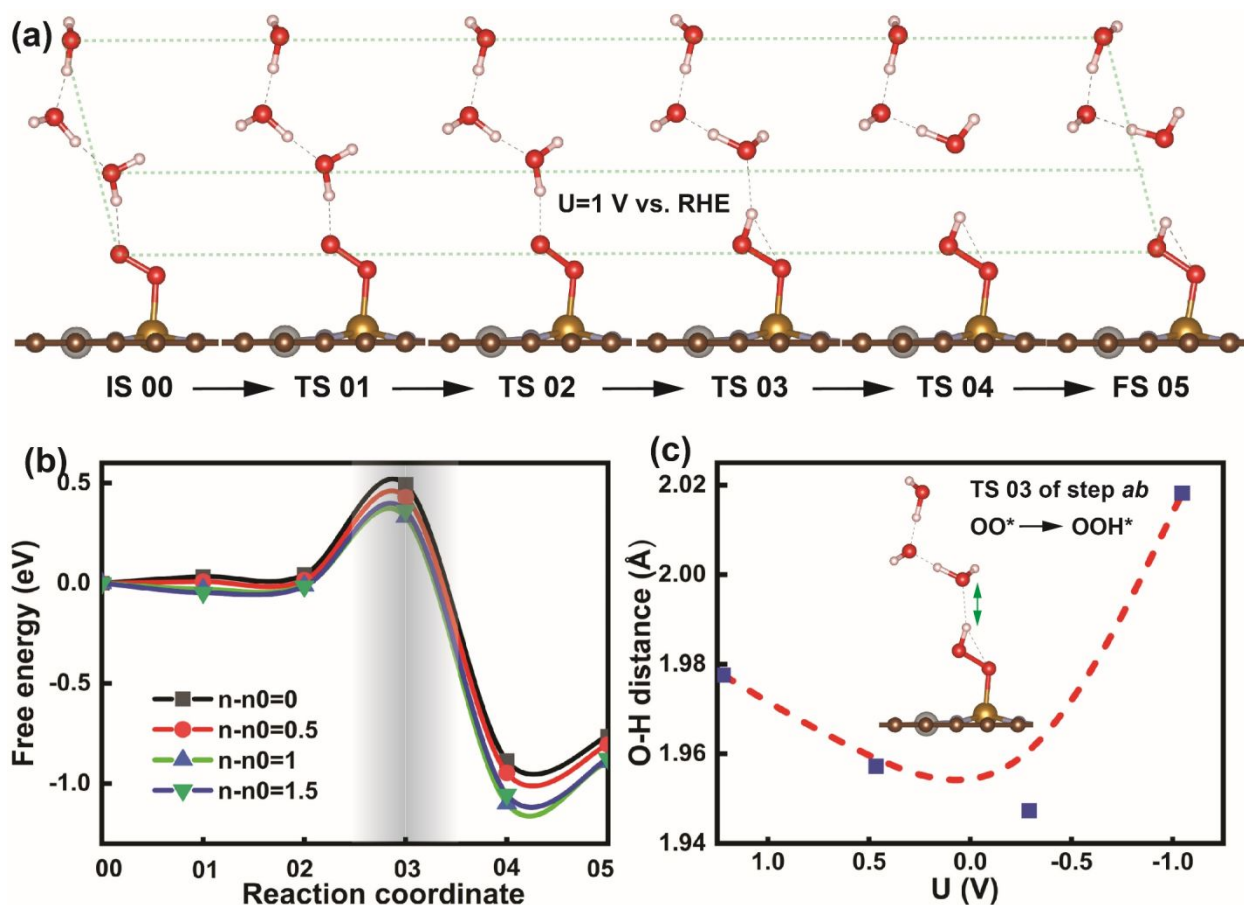
Figure 3. Investigation of transition states of OO*→OOH*. (a) Reaction pathway of step *ab* (OO*→OOH*), indicating the optimized structures of initial, transition, and final states at the applied potential of U=1 V versus RHE. The transition state moves towards final state as more negative potential applied. Four images (01-04) were inserted to search for TS, and 00 and 05 indicate the reactant and product, respectively, *via* minimum energy path (MEP). The dash green lines are to show the atom displacement along the reaction pathway. (b) The free energy barrier for the step 01 ($OO^* \xrightarrow{H^+} OOH^*$) at different numbers of net electrons (n-n_0) in the system. It shows the maximum energy barrier of 0.5 eV and 1.4 eV at net charge of n-n_0=0 e^- for the forward and backward conversion of $OO^* \xrightarrow{H^+} OOH^*$, respectively, on Fe site of FeNiN6-DAC. (c) O-H bond distance variation of TS 03 of step *ab* versus the applied potential.
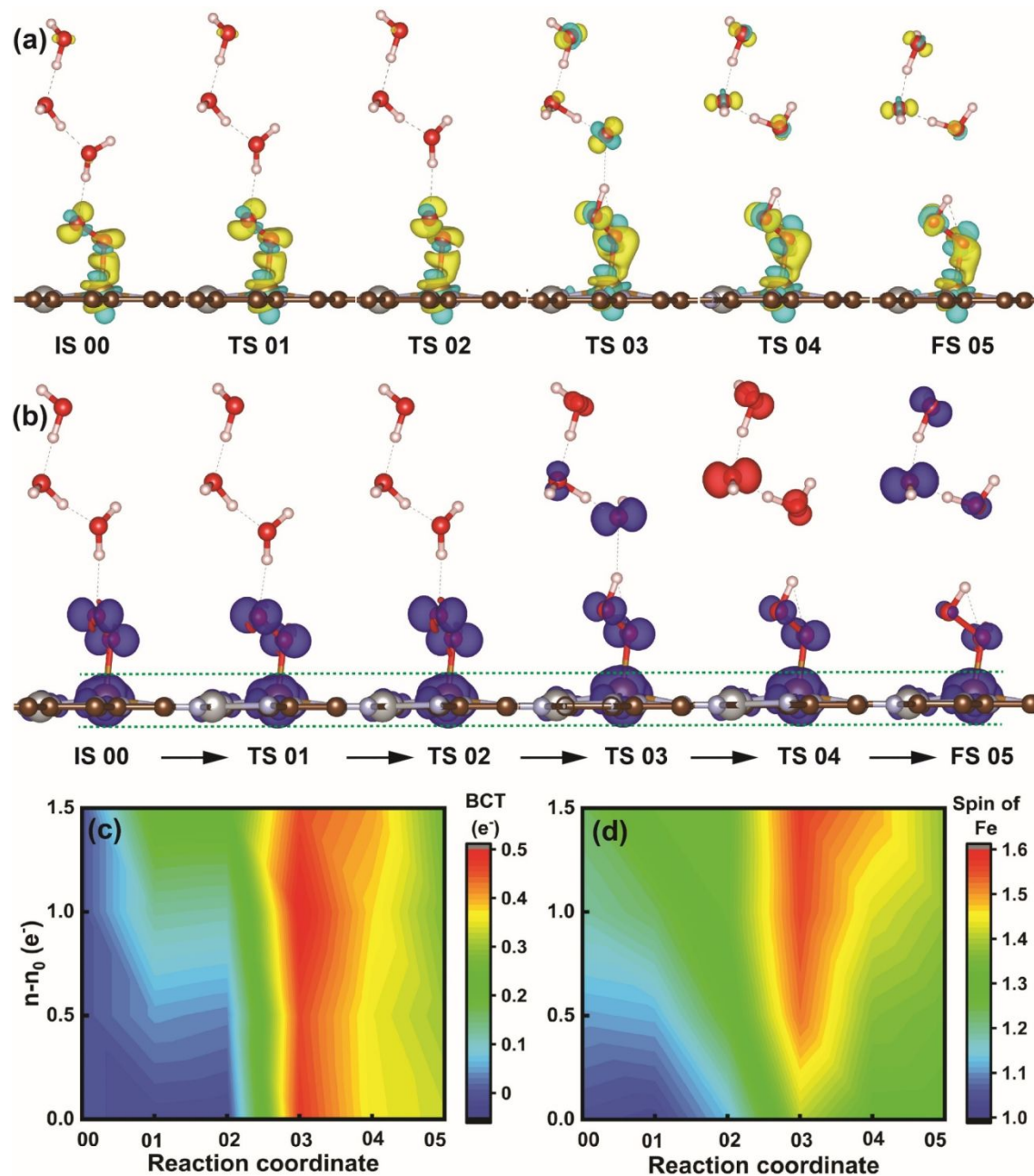
1

2 **Figure 4. Investigation of charge transfer and spin of Fe.** (a) Charge transfer and (b) spin of

3 system along the reaction pathway of step *ab* ($OO^* \xrightarrow{H^+} OOH^*$) at the applied potential of U=1 V

4 versus RHE. This indicates the increase in both charge transfer and spin along the reaction pathway

5 and proton transfer. The dash green line is to show the increase in the spin of Fe atom in the z-axis

6 along the reaction pathway. Contour plot of (c) charge transfer and (d) spin of system vs. net

7 electrons and reaction pathway of $OO^* \xrightarrow{H^+} OOH^*$.

8
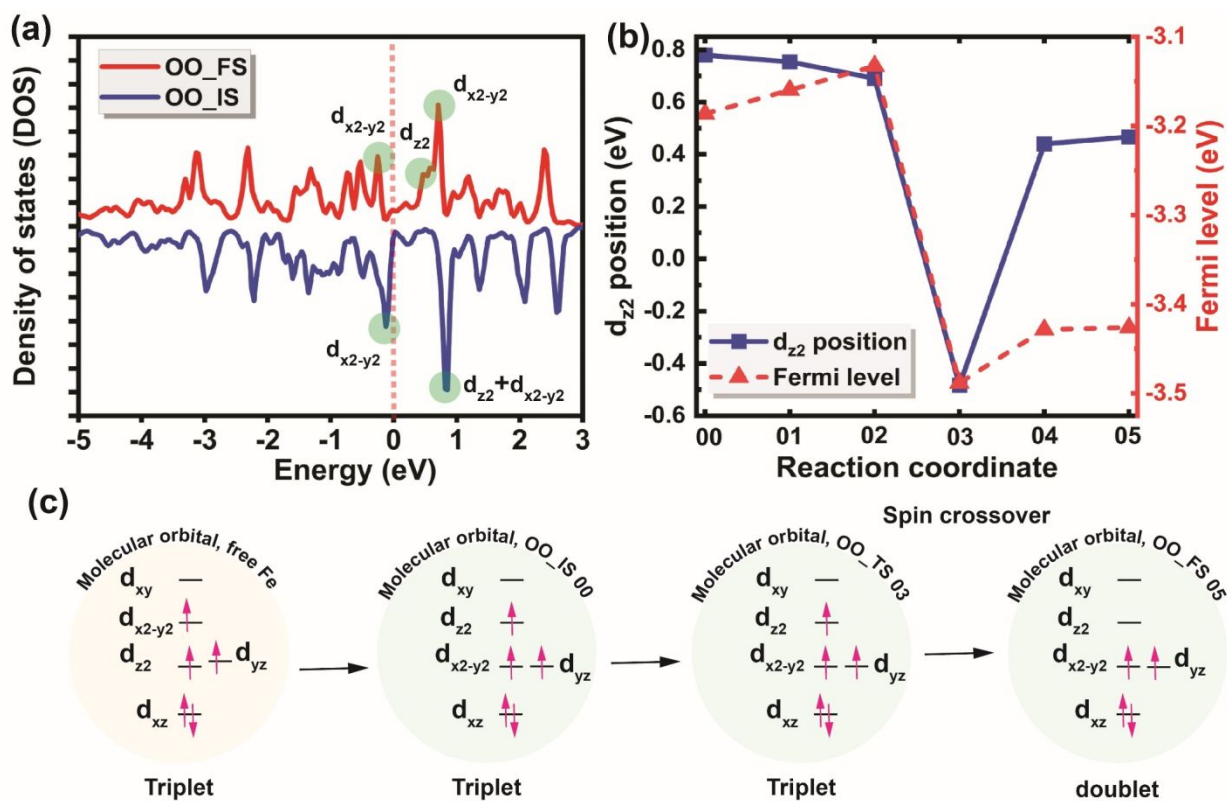
Figure 5. Density of states analysis. (a) The density of states (DOS) of Fe atom in FeNiN6-DAC system for initial and final states of step *ab* ($OO^* \xrightarrow{H^+} OOH^*$), indicating the presence of $3d_{x2y2}$ orbital of Fe atom on the Fermi level. (b) The position of $3d_{z2}$ orbital and Fermi level along the reaction pathway of step *ab* ($OO^* \xrightarrow{H^+} OOH^*$), indicating that both decreases along the proton transfer. (c) The energy level of 3d orbitals of free Fe and Fe-OO* in the initial, transition, and final states of step *ab*, indicating that d_{xy} orbital is empty, d_{x2y2} and d_{z2} orbitals are singly occupied, and d_{xz} and d_{yz} orbitals are doubly occupied.
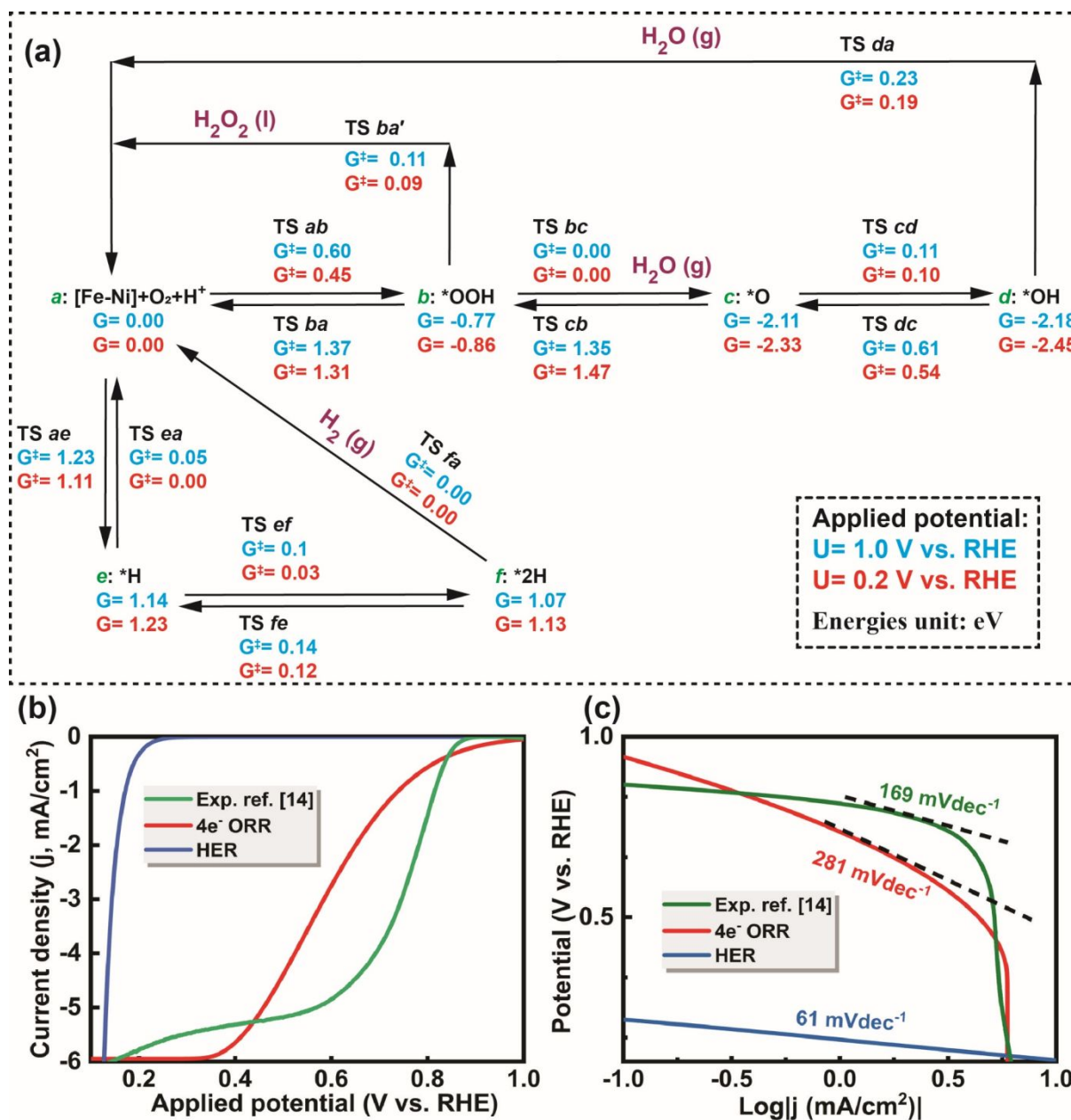
Figure 6. QM derived free energies and predicted reaction kinetics. (a) Schematic representation of free energies at 298.15 K and pH 7 and applied potentials of 1 V versus RHE (blue) and 0.2 V versus RHE (red). This summarizes all reaction intermediates (*a-f*) and transition state (TS) free energies involved in the reduction of O_2 on FeNiN6-DAC at 1 V and 0.2 V constant applied potential. (b) Calculated partial current densities for ORR and HER on FeNiN6-DAC along with experimental data for ORR from ref. [14] (green line) for comparison. (c) Tafel slopes calculated from the I-V curves for ORR and HER on FeNiN6-DAC, showing fair agreement with the experimental ORR Tafel slope from ref. [14] (green line).

1

2
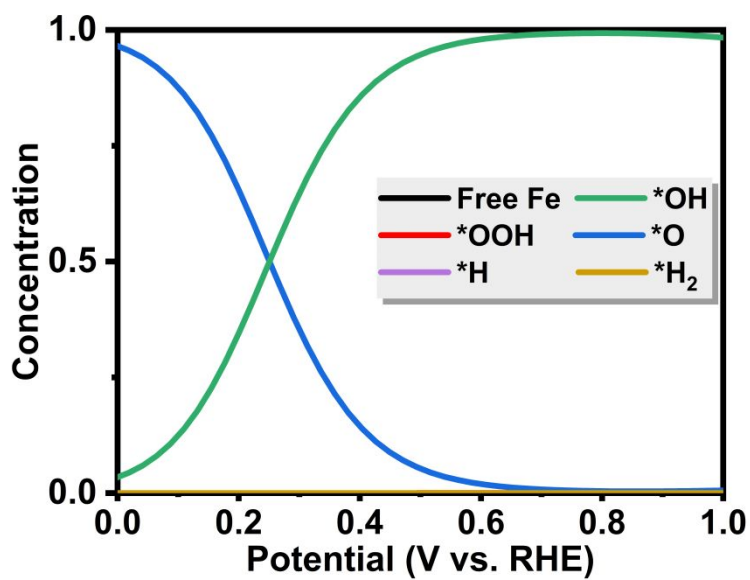
Figure 7. Concentration of ORR intermediates. The change in the concentration of ORR reaction intermediates on the Fe active site of FeNiN6-DAC at different potentials, indicating the dominant coverage of surface with OH* intermediate at higher potentials.

6

7

8